Magnetic Bubbles and Kinetic Alfvén Waves in the High-Latitude Magnetopause Boundary

K. Stasiewicz[1,2], C. E. Seyler[3], F. S. Mozer[4], G. Gustafsson[1], J. Pickett[5] and B. Popielawska[2]
[1]Swedish Institute of Space Physics, Uppsala

[2]Space Research Centre, Polish Academy of Sciences, Warsaw

[3]Cornell University, Ithaca

[4]University of Berkeley, California

[5]Iowa University, Iowa

submitted to Journal of Geophysical Research, 7 July 2000, revised December, 2000.

Short title: MAGNETIC BUBBLES AND KAW

Abstract. We present a detailed analysis of magnetic bubbles observed by the POLAR satellite in the high-latitude magnetopause boundary. The bubbles which represent holes or strong depressions (up to 98%) of the ambient magnetic field are filled with heated solar wind plasma elements and observed in the vicinity of strong magnetopause currents and possibly near the reconnection site. We analyze the wave modes in the frequency range 0-30 Hz at the magnetopause (bubble) layer and conclude that the broadband waves in this frequency range represent most likely spatial turbulence of Kinetic Alfvén Waves (KAW), Doppler shifted to higher frequencies (in the satellite frame) by convective plasma flows. We present also results of a numerical simulation which indicate that the bubbles are produced by a tearing mode reconnection process and the KAW fluctuations are related to the Hall instability created by macroscopic pressure and magnetic field gradients. The observed spatial spectrum of KAW extends from several ion gyroradii ($\sim$ 500 km) down to the electron skin depth ($\sim$ 1 km).

Introduction

Satellites traversing the magnetopause boundary layer, the outer magnetospheric cusp, or the magnetosheath observe frequently regions with strong depressions of the magnetic field, $\delta B/B_0 \sim 90\%$ [*Kaufmann et al.*, 1970; *Tsurutani et al.*, 1982; *Treumann et al.*, 1990; *Lühr and Klöcker*, 1987; *Savin et al.*, 1998]. Similar non-periodic phenomena have been observed in the solar wind [*Turner et al.*, 1977; *Winterhalter et al.*, 1994] and in the magnetospheres of Jupiter [*Tsurutani et al.*, 1993; *Erdös and Balogh*, 1996]. The nature and origin of these structures is not well understood. Although many researchers associate them with mirror-mode instability there are some doubts in the validity of this mechanism [*Tsurutani et al.*, 1999] and explanations in terms of MHD solitary waves have been also suggested [*Baumgärtel*, 1999].

In this paper we present a detailed analysis of magnetic bubbles observed by the POLAR satellite. We find that it is unlikely that the magnetic holes observed at the magnetopause boundary layer are related to mirror mode waves. We present results of a numerical simulation which indicate that the bubbles may be related to tearing mode instability driven by strong magnetopause currents and the smaller scale fluctuations represent kinetic Alfvén waves driven by macroscopic pressure and magnetic field gradients via Hall instability. The results suggest also presence of a turbulent cascade where the energy of KAW cascades through wide range of spatial scales: from a few ion gyroradi $\rho_i \sim 500$ km down to the electron inertial scale $\lambda_e \sim 1$ km.

Observations

Overview of the event April 11, 1997

During periods of high solar wind pressure (5-10 nPa) the orbit of the POLAR spacecraft with the apogee of 9 R_E occasionally crosses the magnetopause current layer and enters the magnetosheath region. In 1996 and 1997 during spring/summer season, when POLAR apogee was on the dayside, the magnetopause crossings were most common in region poleward of the cusp at high-latitudes. One such an event occurred on April 11, 1997, 13:30-15:30 UT when POLAR was in the dusk sector of the high-latitude dayside lobe, GSM (x, y, z)=(2.8, 1.5, 8.0) R_E at 14:30 UT. The ISTP WIND spacecraft was located 230 R_E in front of the Earth and registered solar wind at a steady speed of 450 km/s with the pressure increasing from 5 to 10 nPa, due to the increase of the solar wind number density. During this time interval the IMF was relatively steady with $\mathbf{B}_{GSM}$=(3, -2, 20) nT at WIND position, delayed to POLAR by 56 min. A general configuration of the POLAR orbit during this case can be found in *Russell et al.* [2000].

We shall now focus on the magnetometer data (courtesy of C. Russell) which are shown in Figure 1. The spacecraft was in the high-latitude compressed lobe field of the magnitude of 110 nT until 14:28 UT, when it encountered three Magnetic Bubbles Layers (MBL) seen best in panel B as dropouts of the total magnetic field, marked with solid bars. The bubble layers are located adjacent to the magnetopause current layer best seen as reversals of B_z. The minimum field measured during this event was 1.4 nT which corresponds to 98 % depression of the ambient field of $\sim$ 100 nT. The first bubble layer was followed by a prominent crossing of the magnetopause layer at 14:34 UT and entering into the magnetosheath with nearly oppositely directed magnetic field of similar strength. A sudden change of the B_z and B_x to opposite values at 14:35 UT, accompanied by a decrease of $|B_y|$, is consistent with a high-latitude magnetopause crossing, as the change is toward IMF-like configuration of B_z, a strongly dominating component in the solar wind. Fig 1

The spacecraft re-entered the MBL during 14:43-14:46, returned to the magnetosheath and after another crossing of the MBL and the magnetopause at 14:52 it continued its journey inside the magnetosphere. From the electric field measured by the EFI instrument we compute the $\mathbf{v}_E = \mathbf{E}\times\mathbf{B}/B^2$ velocity for the time interval in Figure 1. The modulus of velocity $\mathbf{v}_E$ is shown in the lowest panel. As can be seen in Figure 1 the $\mathbf{v}_E$ flows are highly variable (50-300 km/s) and significantly higher ($\sim$ 200 km/s) in the bubble layers compared to $\sim$ 80 km/s in the magnetosheath and inside the magnetosphere. The general direction of the convective $\mathbf{v}_E$ and the bulk plasma flow $\mathbf{V}$ (not shown here) are consistent with the expected geometry of flows associated with magnetopause crossing. The GSM v_{Ex} component is positive (sunward) inside the magnetosphere and consistently negative (albeit small) in the magnetosheath "proper" (i.e., in the MS region ouside of the outer part of the MBL, from 14:35:30 to 14:42:00 UT and from 14:47:00 to 14:51:00 UT). Correspondingly, the GSM v_{Ez} component is negative in the magnetosphere and consistently positive in the MS proper. The GSM v_{Ey} component is positive throughout all regions, consistent with the expected flow duskward in the post-afternoon sector of the magnetopause. The bulk plasma flow in the MS proper is sub-Alfvénic, $V < 170$ km/s, antisunward, duskward and poleward, with all 3 components of equal magnitude of about 100km/s (C. Kletzing, private communication). The three bubble layers are characterized by enhanced $\mathbf{v}_E$ flows with increased kinetic energy coming presumably from the redistribution of the ambient magnetic field energy, which can be deduced from high correlation between B and v_E panels in Figure 1.

The characteristics of the electron and ion distributions measured during this event and shown in Figure 2 corroborate the presented above interpretation of the magnetopause crossings. It is seen that the magnetic depressions in Figure 1 are filled with ions and electrons with energy higher than Fig 2

in the adjacent magnetosheath region. The particle energization is accompanied by strong depressions (annihilation) of the magnetic field. The maximum depression of the magnetic field is $\Delta B \approx 100$ nT which corresponds to the magnetic energy density $\Delta B^2/2\mu_0 = 4 \times 10^{-9}$ J/m^3. This magnetic energy is equivalent to particle energy of 800 eV per ion-electron pair at the number density of 30 cm^{-3}. It should be noted here that contrary to our conclusions, some other authors [*Fuselier et al.*, 2000; *Russell et al.*, 2000; *Le et al.*, 2000] do not interpret this case as a magnetopause crossing.

The particle moments show that in the bubble layer the parallel ion and electron pressure exceeds the perpendicular components. This indicates that the condition for the mirror instability [*Southwood and Kivelsen*, 1993]

$$\frac{T_\perp/T_\parallel}{1+\beta_\perp^{-1}} > 1 \qquad (1)$$

is not fulfilled. In Figure 3 we show the plot of the mirror instability condition (1) derived from particle measurements. The plasma is found to be mirror-mode stable in all regions. In Table I we show characteristic plasma parameters in the three main regions of Figure 1: the magnetosheath, bubble layer, and the magnetosphere. Fig.3 Tab I

We now focus on the first bubble layer from Figure 1 which we show in Figure 4. The picture shows that the strong depressions of the magnetic field B are associated with some density variations (on logarithmic scale they do not show very well, see Figure 5 for details), but the very strong density gradient at 1431:15 (first vertical line) is not related to appreciable magnetic perturbations. This density gradient separates obviously the inner magnetosphere from the magnetopause boundary (bubble) layer. On the other hand the magnetic signatures of the magnetopause seen as reversals of B_z at 1434:10 (second vertical line) is not associated with strong density variation. It is, however, associated with strong particle heating leading to a large decrease of total B. In the bottom panel we show the Alfvén velocity Fig 4

$$v_A = \frac{B_0}{(\mu_0\rho)^{1/2}}, \qquad (2)$$

where $\rho = n_i m_i$ is the ion mass density. The ion species is assumed to be hydrogen, and the number density is derived from the "satellite potential" measured by the electric field experiment. We have used an empirical formula derived by [*Escoubet et al.*, 1997], calibrated here with the moments of the particle distributions measured by the HYDRA instrument.

Magnetic bubbles and KAWs

The nature of the observed magnetic bubbles is revealed if we inspect higher resolution plot of two orthogonal components of the magnetic and electric fields shown in Figure 5. High degree of

correlation between B_z and E_y components is characteristic for Alfvén waves. Indeed, for amplitudes $\delta E \approx 30$ mV/m and $\delta B \approx 150$ nT, the ratio $\delta E/\delta B \approx 200$ km/s, which is close to the value for Alfvén velocity v_A inside the bubble layer. The bottom panel shows the electron density derived from the satellite potential (solid line) with superimposed values obtained as moments from the electron and ion measurements (asterisks). One can see good agreement between these two techniques. Fig 5

Let us recall basic properties of Alfvén waves. The original low frequency MHD wave [*Alfvén*, 1942] is dispersionless

$$\omega = k_z v_A, \tag{3}$$

where k_z is the wave vector parallel to the ambient magnetic field. Significant modifications are introduced when the wavelength perpendicular to the background magnetic field becomes comparable either to the ion gyroradius at electron temperature, $\rho_s = (T_e/m_i)^{1/2}/\omega_{ci}$, the ion thermal gyroradius, $\rho_i = (T_i/m_i)^{1/2}/\omega_{ci}$ [*Hasegawa*, 1976], or to the collisionless electron skin depth $\lambda_e = c/\omega_{pe}$ [*Goertz and Boswell*, 1979], where ω_{ci} is ion cyclotron frequency and ω_{pe} is electron plasma frequency.

Recent review by [*Stasiewicz et al.*, 2000*a*] provides a comprehensive discussion on dispersive Alfvén waves in the ionospheric and in laboratory plasmas. In standard terminology, the Inertial Alfvén Waves (IAW) are $\omega < \omega_{ci}$ Alfvén waves in a medium where the electron thermal velocity, $v_{te} = (2T_e/m_e)^{1/2}$, is less than v_A. In such a case, the parallel electric field is supported by the electron inertia. Kinetic Alfvén Waves (KAW) are waves in a medium where $v_{te} > v_A$. In this case, the parallel electric force is balanced by the parallel electron pressure gradient. The term Dispersive Alfvén Waves (DAW) would cover these two cases. Clearly, the IAW arises in a low-beta plasma with $\beta = 2\mu_0 nT/B_0^2 < m_e/m_i$, whereas the KAW appear in an intermediate beta plasma with $m_e/m_i < \beta < 1$. Here, $T = (T_e + T_i)/2$ is the plasma temperature. The low-beta conditions and IAW occur in the topside ionosphere below approximately 1 R_E, whereas at higher altitudes the Alfvén waves have kinetic properties (KAW).

For $\omega < \omega_{ci}$ kinetic Alfvén waves, the well know dispersion equation reads

$$\omega = k_z v_A \sqrt{1 + k_\perp^2(\rho_s^2 + \rho_i^2)}, \tag{4}$$

whereas the E/B ratio for plane, obliquely propagating waves can be expressed as [*Stasiewicz et al.*, 2000*a*]

$$\left|\frac{\delta E_y}{\delta B_x}\right| = \frac{v_A(1 + k_\perp^2\rho_i^2)}{[1 + k_\perp^2(\rho_s^2 + \rho_i^2)]^{1/2}} \approx v_A\sqrt{1 + k_\perp^2\rho_i^2}. \tag{5}$$

In the above approximation we have used the experimental condition $T_i/T_e \approx 8$ which implies $\rho_i \gg \rho_s$.

An analysis of the E/B ratio performed for IAW measured by Freja at lower altitudes [*Stasiewicz et al.*, 2000*b*] has demonstrated that broadband ELF waves (BB-ELF) observed in the frequency range

0-500 Hz represent in fact spatial turbulence of dispersive Alfvén waves. Simply, waves $\omega \ll \omega_{ci}$ with a spectrum of spatial scales $\Delta\mathbf{k}$ (such that $k = 2\pi/\lambda$) are recorded on a moving spacecraft as waves in the frequency domain

$$\Delta\omega_d = \mathbf{v} \cdot \Delta\mathbf{k}, \tag{6}$$

where $\mathbf{v}$ is velocity of the plasma structure with respect to the satellite. Distinction between true time-domain waves $\Delta\omega$ and Doppler shifted spatial waves $\Delta\mathbf{k}$ can be done directly with multiple probe measurements, or indirectly with the help of the dispersion relation (5) as has been done by [*Stasiewicz et al.*, 2000*b*] for waves measured by Freja. The dispersion relation for IAW is similar to (5) with collisionless electron skin depth λ_e instead of ion gyroradius ρ_i. Additional difference between the Freja and POLAR cases is that the convective flows at Freja altitudes (∼1500 km) are much smaller than the satellite velocity so $v \approx v_s \approx 7$ km/s in equation (6). On the other hand at POLAR apogee, the satellite speed $v_s \approx 3$ km/s is much smaller than convective flows, and $v \approx \mathbf{v}_E \approx 100$ km/s. DAW spectrum $\Delta\mathbf{k}$ described by equation (5) should be observed on a spacecraft as a frequency spectrum

$$\left|\frac{\delta E_y}{\delta B_x}\right| \approx \langle v_A \rangle \sqrt{1 + \left\langle \frac{2\pi\rho_i}{v\cos\theta} \right\rangle^2 f^2}, \tag{7}$$

where $f(= \mathbf{k}\cdot\mathbf{v}/2\pi)$ is an apparent Doppler frequency in the satellite frame, θ is the angle between the $\mathbf{k}$-vector and the velocity $\mathbf{v}$, and brackets $\langle\rangle$ represent a spatial average. Fig 6

In Figure 6 we show average power spectrum of the electric field fluctuations measured in the frequency range 0-10^4 Hz and the ratio $\delta E/\delta B$ as a function of frequency. To make these plots we took continuous dc field and snapshot measurements at higher frequencies within the bubble layers marked in Figure 1. The frequency spectrum is covered by three instruments. The dc magnetic field is sampled continuously at the rate 8.3 s^{-1}, the low-frequency waveform receiver (LFWR) and high-frequency waveform receiver (HFWR) provide snapshots sampled at the rate 100 s^{-1}, and 50,000 s^{-1}, respectively. The plots of dc and LFWR channels overlap completely indicating good inter-calibration. However, because of the wave instrument filter characteristics the plots in Figure 6 at the transition frequency of ∼ 50 Hz between LFWR and HFWR are not reliable. Anyway, the power spectrum and the waveforms show that the dominant mode represent broadband ELF waves 0-30 Hz with a significant power drop above ∼30 Hz, which is near the lower hybrid range.

The asterisk curve shows equation (7) computed for $v_A = 150$ km/s and $\rho_i/v = 0.4$ s, which is satisfied for e.g. $\rho_i = 60$ km and $v = 150$ km/s, $\langle\cos\theta\rangle \sim 1$. A good agreement between approximation (7) and the measurements provides indirect evidence that in the frequency range 0-30 Hz the waves represent spatial turbulence of DAW. Transition from equation (5) to (7) requires knowledge of the

angle between the convection velocity $\mathbf{v}_E$ and the wavevector $\mathbf{k}$. Because both these vectors are expected to vary significantly in time (space) we use here statistical average of spectra which would result in an average value for $\langle \cos\theta \rangle$ and other parameters in equation (7).

Translation from frequency to spatial scale $\lambda = v/f$ requires the knowledge of the convective velocity v. For $v \approx$100 km/s, the frequency of 1 Hz corresponds to $\lambda =$100 km which is on the order of ion gyroradius, while 100 Hz corresponds to $\lambda \approx 1$ km, which is about the electron inertial length. It appears from Figure 6 that for scales larger than ρ_i waves have $\delta E/\delta B \approx v_A$, while the dispersive KAW spectrum (7) extends from ρ_i down to λ_e. Above 30 Hz, or close to the inertial electron scale, dissipative processes related presumably to electron acceleration lead to the dropout of the electric field power seen in Figure 6. The bubble structures correspond roughly to ~ 0.2 Hz. It is interesting to note that the ordering of scales ρ_i and λ_e is reversed at low altitudes and DAW waves measured on Freja extends from $\lambda_e \sim 300$ m down to $\rho_i \sim 20$ m, where they are strongly dissipated due to stochastic acceleration of ions [*Stasiewicz et al.*, 2000*b*; *Stasiewicz et al.*, 2000*c*].

Theory and simulation

The discussion on linear spectra for KAW in the previous section could not address the origin of the observed large amplitude structures. Since the kinetic Alfvén wave carry a parallel and perpendicular electric field they can accelerate ions and electrons along as well as perpendicular to the magnetic field. The nonlinear interaction with quasi-stationary density and compressional magnetic field perturbations can gives rise to modulational instability. Even the linear small amplitude DAW become compressional for sufficiently large $k_\perp$. Indeed, the density fluctuations depend on the $k_\perp \lambda_i$, where $\lambda_i = v_A/\omega_{ci} = c/\omega_{pi}$ is the inertial ion length, as [*Hollweg*, 1999]

$$\frac{\delta n_i}{n_0} = k_\perp \lambda_i \frac{v_E}{v_A}. \tag{8}$$

The above result applies both to KAW and IAW and shows that the Alfvén wave becomes compressible when perpendicular size of the structures becomes comparable to the inertial ion length. In our case, it is seen from Table I that the wave induced convective flows are comparable to the Alfvén velocity and the density perturbations implied by (8) may be quite large, as seen in Figure 5.

The density fluctuations imply pressure fluctuations that drive a magnetization current, which in turn produces a compressive magnetic field δB_z. In the linear approximation the density and compressional magnetic field fluctuations are related as [*Hollweg*, 1999]

$$\frac{\delta B_z/B_0}{\delta n_i/n_0} = -\frac{c_s^2}{v_A^2}, \tag{9}$$

where c_s is the ion sound speed. The observed values for c_s can be obtained from Table I as $v_s = v_i\sqrt{T_e/T_i}$, i.e., they are 2-3 times smaller than v_i.

The parallel electric field of KAW will affect particles which are in Landau resonance with the wave

$$k_z v_z = \omega. \tag{10}$$

Table I shows that both ion thermal and bulk flow is on the order of the Alfvén speed. Thus, one expects efficient ion heating via Landau resonance which can account for ion energization seen in Figure 2.

The linear theory has a limited application to the strongly nonlinear structures seen in the measurements. We present here results from the solution of the resistive Hall MHD equations which are intended to model a tearing mode reconnection process leading to magnetic bubble or island formation which are associated with kinetic Alfvén wave fluctuations. We present the general resistive Hall MHD equations then specialize to the two-dimensional geometry that we use in the simulations. The Hall instability which is related to drift Alfvén waves is discussed in the context of the two-dimensional model for which it is shown that instability exists at scales smaller than the tearing mode scale. A sample simulation of high spatial resolution is presented which exhibits the formation of magnetic islands through the tearing mode and kinetic Alfvén wave fluctuations through the Hall instability.

Hall MHD Model

The Hall MHD equations are:

$$\partial_t n + \nabla \cdot (n\mathbf{u}) = 0 \tag{11}$$

$$(\partial_t + \mathbf{u}\cdot\nabla)\mathbf{u} = -\frac{1}{\rho}\nabla p + \frac{1}{\mu_0\rho}(\nabla\times\mathbf{B})\times\mathbf{B} \tag{12}$$

$$(\partial_t + \mathbf{u}\cdot\nabla)\, p + \gamma p \nabla\cdot\mathbf{u} = 0 \tag{13}$$

$$\partial_t \mathbf{B} = -\nabla\times\mathbf{E} \tag{14}$$

$$\mathbf{E} + \mathbf{u}\times\mathbf{B} = \frac{1}{\mu_0 ne}(\nabla\times\mathbf{B})\times\mathbf{B} + \eta\mathbf{J} \tag{15}$$

$$\nabla\times\mathbf{B} = \mu_0\mathbf{J} \tag{16}$$

where n is the number density, $\rho = Mn$ is the mass density, M is the mean particle mass, $\mathbf{u}$ is the fluid velocity, p is the pressure, $\mathbf{B}$ is the magnetic field, $\mathbf{J}$ is the current density, $\mathbf{E}$ is the electric field, η is the resistivity and γ is the adiabatic constant for which we use $\gamma = 2$ in our simulations.

Two-dimensional dimensionless equations

The equations are nondimensionalized as follows: The fluid velocities are normalized to the characteristic Alfvén speed $v_A = B_0/\sqrt{\rho_0 \mu_o}$, mass density to the ambient mass density ρ_0, length scales to a characteristic length L and time scales to L/v_A. We consider two-dimensional variations in the $x - z$ plane where the y direction is ignorable. In two dimensions when expressed in term of the vector potential $\mathbf{B} = \hat{y}B_y - \hat{y} \times \nabla A_y$ the electric field components become

$$E_x = u_y\, \partial_x A_y + u_z\, B_y - \frac{\epsilon}{n}\left[\frac{1}{2}\, \partial_x (B_y)^2 + \partial_x A_y \nabla^2 A_y\right] - \eta \partial_z B_y \tag{17}$$

$$E_y = u_x\, \partial_x A_y + u_z\, \partial_z A_y + \frac{\epsilon}{n}\left(\partial_x A_y\, \partial_z B_y - \partial_z A_y\, \partial_x B_y\right) - \eta \nabla^2 A_y \tag{18}$$

$$E_z = u_y\, \partial_z A_y - u_x\, B_y - \frac{\epsilon}{n}\left[\frac{1}{2}\, \partial_z (B_y)^2 + \partial_z A_y \nabla^2 A_y\right] + \eta \partial_x B_y \tag{19}$$

where $\epsilon = \lambda_i/L$ is the Hall parameter and $\lambda_i = c/\omega_{pi}$. The components of the momentum equation are

$$\partial_t u_x + (u_x \partial_x + u_z \partial_z) u_x = -\frac{1}{\rho}\left[\partial_x \left(p + \frac{1}{2}\, B_y^2\right) + \partial_x A_y \nabla^2 A_y\right] \tag{20}$$

$$\partial_t u_y + (u_x \partial_x + u_z \partial_z) u_y = \frac{1}{\rho}\left(\partial_x A_y\, \partial_z B_y - \partial_z A_y\, \partial_x B_y\right) \tag{21}$$

$$\partial_t u_z + (u_x \partial_x + u_z \partial_z) u_z = -\frac{1}{\rho}\left[\partial_z \left(p + \frac{1}{2}\, B_y^2\right) + \partial_z A_y \nabla^2 A_y\right] \tag{22}$$

The components of Faraday's law are

$$\partial_t A_y = -E_y \tag{23}$$

$$\partial_t B_y = \partial_x E_z - \partial_z E_x \tag{24}$$

Finally the continuity and pressure equations are

$$\partial_t \rho + \partial_x (\rho u_x) + \partial_z (\rho u_z) = 0 \tag{25}$$

$$\partial_t p + u_x \partial_x p + u_z \partial_z p + \gamma p \left(\partial_x u_x + \partial_z u_z\right) = 0 \tag{26}$$

Equations (17) - (26) are the complete two-dimensional Hall MHD equations.

Hall instability

The Hall equations can exhibit instability in the presence of equilibrium electric field created by equilibrium pressure and magnetic field gradients. We perform a local analysis of (17) - (26) assuming perturbations of the form $\exp[ik_z z - i\omega t]$. After considerable algebra we find

$$(\omega^2 - k_z^2 v_A^2)(\omega - k_z v_E) + \omega(\omega^2 - k_z^2 c_s^2) k_z \lambda_i^2 = 0 \tag{27}$$

where $v_E = E_{0x} B_{0y}/B_0^2$ and $c_s^2 = \gamma p_0/\rho_0$. Equation (27) has unstable roots for $v_E > c_s$ and within a band limited range of wavenumbers. When $v_E = 0$ the dispersion relation becomes

$$\omega^2 = \frac{k_z^2 v_A^2 (1 + k_z^2 \rho_s^2)}{1 + k_z^2 \lambda_i^2} \tag{28}$$

where $\rho_s = c_s/\Omega_i$. Equation (28) is the dispersion relation for Alfvén-ion cyclotron waves. For $k_z \lambda_i \ll 1$ it reduces to pure kinetic Alfvén waves. The local approximation does not allow us to consider $k_x \neq 0$ since the equilibrium varies in the x direction although the simulation does of course allow nonzero k_x. For the homogeneous case we can allow $k_x \neq 0$ and we find for $k_z \lambda_i \ll 1$, the dispersion relation $\omega^2 = k_z^2 v_A^2 (1 + k^2 \rho_s^2)$, where $k^2 = k_x^2 + k_z^2$, which is more typically considered to be the kinetic Alfvén wave dispersion relation. For $v_E > c_s$ there is a band of wavenumbers that are unstable. This instability has been discussed in the context of cold laboratory plasma by *Gordeev et. al* [1994] and warm laboratory plasma by *Maggs and Morales* [1996]. The instability given by (27) is due to the interaction between the drift mode $\omega = k_z v_E$ and the Alfvén-ion cyclotron mode given in (28). The acoustic speed is stabilizing and the threshold condition is $v_E > c_s$. A local analysis can be misleading in a sheared magnetic field such as we consider here. This is because the shear limits the x extent of the mode thereby significantly altering the stability properties. A nonlocal analysis is required to obtain quantitative estimates of the growth rate. That analysis is beyond the scope of the present paper and will be deferred to a future publication.

Simulation results

We present the results of one simulation to show the magnetic bubble structure and the fluctuations associated with the Hall instability. The simulation is not intended to reproduce the observations in any detail but only to show that with reasonable initial conditions spontaneous reconnection in the form of a tearing mode will result and that instability associated with the large gradients of the bubble boundary will arise from the Hall instability. This should be considered in comparing the simulation

results to the data.

The simulation code is based upon the Fourier spectral method and is similar to that described in *Seyler* [1990]. The equations are solved in dimensionless form with the following non-dimensional tilded variables: $\tilde{t} = tL/v_A$, $\tilde{\mathbf{x}} = \mathbf{x}/L$, $\tilde{\mathbf{u}} = \mathbf{u}/v_A$, $\tilde{\mathbf{B}} = \mathbf{B}/B_0$, $\tilde{P} = P/P_0$, and $\tilde{\rho} = \rho/\rho_0$, where L is the characteristic scale of the equilibrium. From these one can revert from simulation to physical units. The simulation dimensions are $-\pi < x \leq \pi$ and $-2\pi < z \leq 2\pi$. The Hall parameter is $\epsilon = 0.026$. The number of grid points used are 128 in x and 256 in z. The time step is $\Delta t = 0.0025$. The initial equilibrium is of the form $J_y(x) = J_0 \operatorname{sech}(-ax^2)$, where $J_0 = 8$ and $a = 4\pi$. The dimensionless resistivity is $\eta = 0.002$. The dimensionless current layer width a was chosen to produce an tearing mode unstable current layer that grows to form fully developed bubbles in a time comparable to the Hall instability growth time. Fig 7

The current density is shown in Figure 7. The magnetic bubbles are the two magnetic islands formed by the tearing mode. The kinetic Alfvén wave fluctuations are readily apparent. The contour plot of $B_y(x, z)$ is shown in Figure 8. This plot clearly shows the vortices associated with the flow due to the Hall instability. The fluctuations due to the Hall instability are concentrated on the bubble boundaries since that is where the magnetic field gradient is largest. Figures 1 and 4 also show that magnetic fluctuations are enhanced near the bubble boundaries. This is consistent with the interpretation that the fluctuations are the result of the Hall instability which is driven by the magnetic gradient. Fig 8

The plots shown in Figures 9 and 10 are taken along z at 4 grid points to the right of the centerline of the simulation region. They show the relative level of variation of the magnetic field, pressure and density. Fig 9

Figure 9 shows the magnetic bubble from the perspective of a one-point satellite measurement and can be compared to Figure 4 (of the observational section). The best comparison is obtained when the simulation B_x is compared to the observed B_y and when the simulation z coordinate has a significant component in the data x direction. Given the POLAR GSM coordinates, $(x, y, z) = (2.8, 1.5, 8.0)\, R_E$, this correspondence is reasonable, since the simulation uses coordinates appropriate to the magnetopause located approximately at $(x, y, z) = (10, 0, 0)\, R_E$. Fig 10

Figure 10 shows that the region inside the magnetic bubble or island is significantly hotter than the outside region. This is due to the fact that the initial pressure at $x = 0$ must be larger to create pressure balance with the equilibrium magnetic field. Since we chose the initial density to be constant, this implies the temperature is hottest initially at $x = 0$. The evolution of the pressure is such that

the temperature is hottest in the center of the magnetic island. This is not surprising since the tearing mode evolves quasi-statically in that the growth time is much less that the Alfvén time. Therefore quasi-static pressure balance requires that the pressure has a maximum where the magnetic field magnitude is a minimum. Thus the increase of the plasma pressure is due to the compensation the magnetic field depression, so that the total pressure is approximately constant.

The tearing mode instability has been discussed by numerous authors the list of which is too extensive to give here. Much of the relevant literature is referenced in the review article by [*White*, 1986]. The tearing mode is spontaneous reconnection that lowers the magnetic energy of the initial equilibrium state. The formation of magnetic islands is characteristic of the tearing mode. A magnetic island is a region of closed contours of the vector potential which typically has a lower field at the center of the island. Magnetic islands form as the result of the reconnection flow in which the plasma is advected towards the separatrix by the inflow and exhausted into the region inside the separatrix by the outflow jets thereby filling the region inside the separatrix with plasma and forming a magnetic bubble. The magnetic energy is lowered and converted into kinetic energy in this process. The amount the initial magnetic energy is lowered depends considerably upon the plasma parameters and the initial conditions, but about 10% is typical [*Steinholfson and Van Hoven*, 1984]. The redistribution of the magnetic energy density can vary greatly between the outside and inside regions of the island. The POLAR observation of more than 90% is not unreasonable and is close to what was found in the simulation.

Discussion and Conclusions

A detailed analysis of electromagnetic and plasma properties of magnetic holes observed in the vicinity of the magnetopause layer supplemented by a numerical simulation show that these are most likely related to tearing mode instability which develops strongly nonlinear structures on the scale of the current layer width.

We have demonstrated that the $\delta E/\delta B$ ratio for large scale features is close to the Alfvén velocity, indicating that these can be regarded as nonlinear Alfvén wave structures. For smaller scale structures this ratio gradually increases and it is well represented by the dispersion relation for KAWs (see Figure 6). Thus, the measurements suggest that broadband waves observed at the magnetopause layer in the frequency range 0.1-30 Hz represent most likely spatial turbulence of nonlinear and dispersive Alfvén waves ($\lambda_\perp \approx 1500 - 5$ km and $\omega \ll 1$ Hz), which are Doppler shifted to the observed frequencies by convective plasma flows $v_E \sim 150$ km/s.

The numerical simulation indicates that the small scale KAW may be generated through the Hall instability on the macroscopic pressure and magnetic field gradients produced by the tearing mode driven by strong magnetopause currents. The presented particle measurements indicate that both ions and electron are energized to about twice their initial energy inside the magnetopause bubble layer. The particle energization could be related to kinetic Alfvén waves which cover the spatial scales ranging from λ_i, ρ_i down to λ_e and thus can interact and energize both with ions and electrons. The magnetic fluctuation are likely due to a drift-Alfvén type instability. We have only presented a limited analysis and more work is necessary to have complete understanding of the fluctuations. The simulation model is limited to two-dimensions. This in itself restricts the possible types of instabilities. Since the current due to reconnection is in the ignorable direction of the simulation, these instabilities would not accounted for in the model. To include these would require a three dimensional model. The solution of a three-dimensional model at the required resolution is beyond our capabilities at this point in time. A linear stability analysis, however is tractable and will be reported upon in a future paper.

The processes discussed in this paper involve transformations of considerable amount of energy between the magnetic, electric fields and particles (thermal and translational). For example we observe a reduction of 98% of the magnetic energy inside some bubbles. Consequently, full understanding of the processes discussed in this paper is of fundamental importance for the energetics of the solar wind - magnetosphere coupling.

Acknowledgments. The authors would like to thank C. Kletzing for providing the HYDRA data and principal investigators: D. Gurnett, C. T. Russell and J. Scudder for making available the field and plasma measurements. Work of F.S. Mozer was partly supported by NASA grant FDNAG5-8078 and B.Popielawska was supported by KBN grant 2.P03C.004.13.

References

Alfvén, H., Existence of electromagnetic-hydromagnetic waves, *Nature*, *150*, 405–406, 1942.

Baumgärtel, K., Soliton approach to magnetic holes, *J. Geophys. Res.*, *104*, 28295, 1999.

Erdös, G., and A. Balogh, Statistical properties of mirror mode structures observed by Ulysses in the magnetosheath of Jupiter, *J. Geophys. Res.*, *101*, 1–12, 1996.

Escoubet, C. P., A. Pedersen, R. Schmidt, and P. A. Lindqvist, Density in the magnetosphere inferred from ISEE 1 spacecraft potential, *J. Geophys. Res.*, *102*, 17,595, 1997.

Fuselier, S. A., K. J. Trattner, and S. M. Petrinec, Cusp observations of high- and low-latitude reconnection for northward IMF, *J. Geophys. Res.*, *105*, 253-266, 2000.

Goertz, C. K., and R. W. Boswell, Magnetosphere-ionosphere coupling, *J. Geophys. Res.*, *84*, 7239–7246, 1979.

Gordeev, A. V., A. S. Kinsep, and L. I. Rudakov, Electron magnetohydrodynamics, *Phys. Rep.*, *243*, 215–315, 1994.

Hasegawa, A., Particle acceleration by MHD surface wave and formation of aurora, *J. Geophys. Res.*, *81*, 5083–5090, 1976.

Hollweg, J. V., Kinetic Alfvën wave revisited, *J. Geophys. Res.*, *104*, 14,811, 1999.

Kaufmann, R., J. T. Horng, and A. Wolfe, Large amplitude hydromagnetic waves in the inner magnetosheath, *J. Geophys. Res.*, *75*, 4666, 1970.

Le, G., J. Raeder, C. T. Russell, G. Lu, S. M. Petrinec, and F. S. Mozer, Polar cusp and vicinity under strongly northward IMF on April 11, 1997: Observations and MHD simulations, *J. Geophys. Res.*, *xx*, in press, 2000.

Lühr, H., and N. Klöcker, AMPTE IRM observations of magnetic cavities near the magnetopause, *Geophys. Res. Lett.*, *14*, 186, 1987.

Maggs, J. E., and G. J. Morales, Magnetic fluctuations associated with field-aligned striations, *Geophys. Res. Lett.*, *23*, 633, 1996.

Russell, C. T., G. Le, and S. M. Petrinec, Cusp observations of high- and low-latitude reconnection for northward IMF: An alternate view, *J. Geophys. Res.*, *105*, 5489-5495, 2000.

Savin, S. P., et al., The cusp/magnetosheath interface on May 29, 1996: Interball-1 and Polar observations, *Geophys. Res. Lett.*, *25*, 2963, 1998.

Seyler, C. E., A mathematical model of the structure and evolution of small-scale discrete auroral arcs, *J. Geophys. Res.*, *95*, 17199, 1990.

Southwood, D. J., and M. G. Kivelsen, Mirror instability 1, the physical mechanism of linear instability, *J. Geophys. Res.*, *98*, 9181, 1993.

Stasiewicz, K., P. Bellan, C. Chaston, C. Kletzing, R. Lysak, J. Maggs, O. Pokhotelov, C. Seyler, P. Shukla,

L. Stenflo, A. Streltsov, and J.-E. Wahlund, Small scale Alfvénic structure in the aurora, *Space Sci. Rev.*, *92*, 423-533, 2000*a*.

Stasiewicz, K., Y. Khotyaintsev, M. Berthomier, and J.-E. Wahlund, Identification of widespread turbulence of dispersive Alfvén waves, *Geophys. Res. Lett.*, *27*, 173, 2000*b*.

Stasiewicz, K., R. Lundin, and G. Marklund, Stochastic ion heating by orbit chaotization on electrostatic waves and nonlinear structures, *Phys. Scripta*, *T84*, 60, 2000*c*.

Steinholfson R. S. and G. V. Van Hoven, Nonlinear Evolution of the Resistive Tearing Mode, *Phys. Fluids*, *27*, 1207, 1984.

Treumann, R., L. Brostrom, J. LaBelle, and N. Scopke, The plasma waave signature of a magnetic hole in the vicinity of the magnetopause, *J. Geophys. Res.*, *95*, 19,099, 1990.

Tsurutani, B. T., E. J. Smith, R. R. Anderson, K. W. Ogilvie, J. D. Scudder, D. N. Baker, and S. J. Bame, Lion roars and nonoscillatory drift mirror waves in the magnetosheath, *J. Geophys. Res.*, *87*, 6060, 1982.

Tsurutani, B. T., J. Arballo, E. J. Smith, D. Southwood, and A. Balogh, Large amplitude magnetic pulses downstream of the jovian bow shock, *Planet. Space Sci.*, *41*, 851, 1993.

Tsurutani, B. T., G. S. Lakhina, D. Winterhalter, J. Arballo, G. Galvan, and R. Sukurai, Energetic particle cross-field diffusion: Interactions with magnetic decreases, *Nonlinear Proc. in Geophys.*, *6*, 235, 1999.

Turner, J. M., L. F. Burlaga, N. F. Ness, and J. F. Lemaire, Magnetic holes in the solar wind, *J. Geophys. Res.*, *82*, 1921, 1977.

White, R. B., Resistive Reconnection, *Rev. Mod. Phys.*, *58*, 183, 1986.

Winterhalter, D., M. Neugebauer, B. E. Goldstein, E. J. Smith, S. J. Bame, and A. Balogh, Ulysses field and plasma observations of magnetic holes in the solar wind and their relation to mirror-mode structures, *J. Geophys. Res.*, *99*, 23,371, 1994.

Received _____

Table 1. Plasma parameters in three regions of Figure 2. Parameters not defined in text are: $\lambda_i = c/\omega_{pi}, f_{ce}$ electron gyrofrequency, f_{pi}, f_{ci} ion (proton) plasma and gyro-frequency, f_{LH} lower-hybrid frequency.

	n	B	T_e	T_i	v_E	v_i	v_A	λ_e	ρ_i	λ_i	β	f_{ci}	f_{LH}	f_{pi}
	cm^{-3}	nT	eV	eV	km/s	km/s	km/s	km	km	km		Hz	Hz	kHz
Sheath	25	100	20	150	100	150	400	1	20	50	0.1	1.4	65	1
Bubble	15	50	50	400	200	300	200	1	80	60	1	0.7	32	1
Sphere	0.2	110	80	800	50	400	5000	10	40	500	10^{-3}	1.5	60	0.1

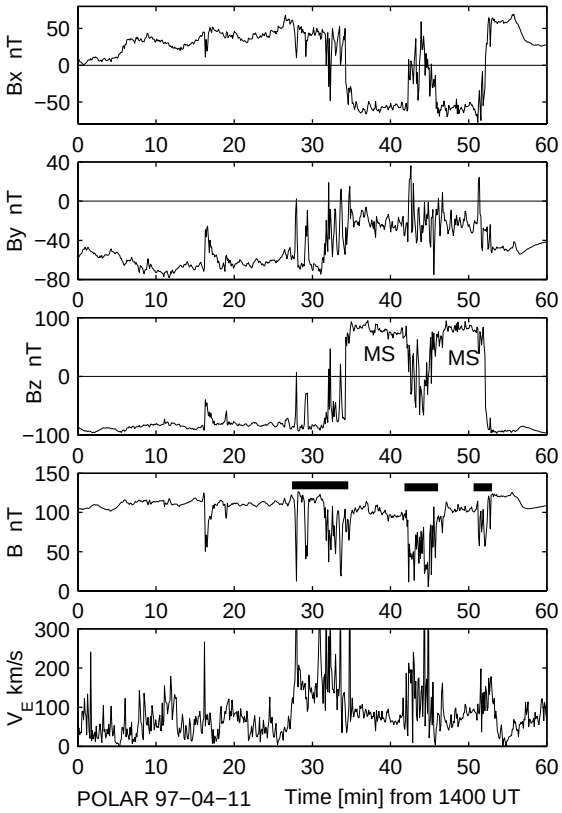

Figure 1. Magnetopause crossings on 11 April 1997. Three component magnetic field B_x, B_y, B_z in GSM coordinates, $|B|$ and the convection speed v_E.

Figure 2. Particle distributions measured during the analyzed event. Three electron and three ion panels show particle fluxes along the magnetic field, perpendicular, and antiparallel to **B**. The magnetosheath and bubble layers are marked with MS and B, respectively.

Electron energy [eV]

10^4 10^3 10^2

HYDRA Ele ⊥ 75<α<105

10^8 10^7 10^6 10^5

B ---- B ----- MS --- B --- MS -B

Ion energy [eV]

10^4 10^3 10^2

HYDRA Ion ⊥ 75<α<105

10^7 10^6 10^5

14:00 14:15 14:30 14:45 15:00

April 11, 1977

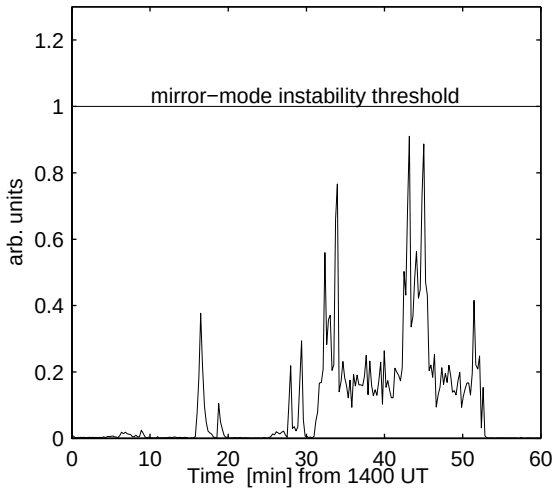

Figure 3. The mirror-mode instability condition (1) derived from particle measurements. The plasma is mirror-mode stable in all regions: the magnetosheath, bubble layer and the magnetosphere.

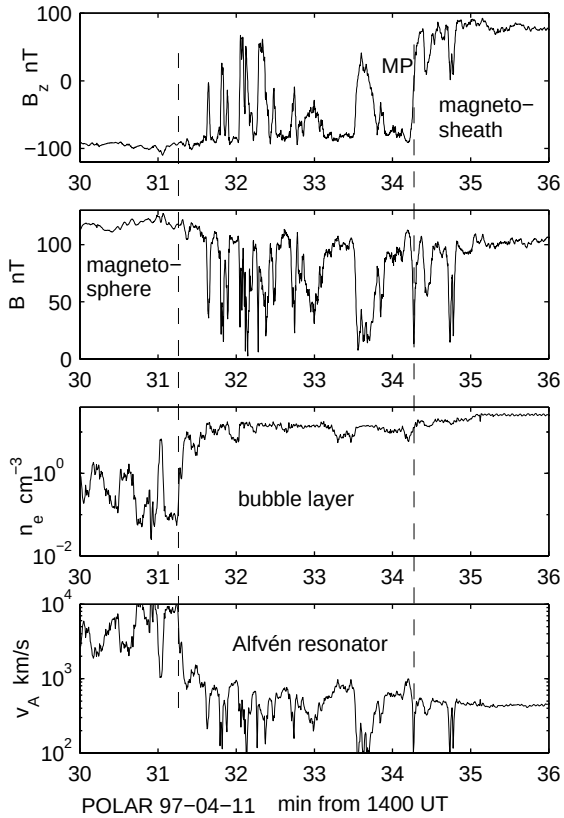

Figure 4. Details of a bubble layer: magnetic field B_z and B, the electron density n_e, and the Alfvén velocity v_A.

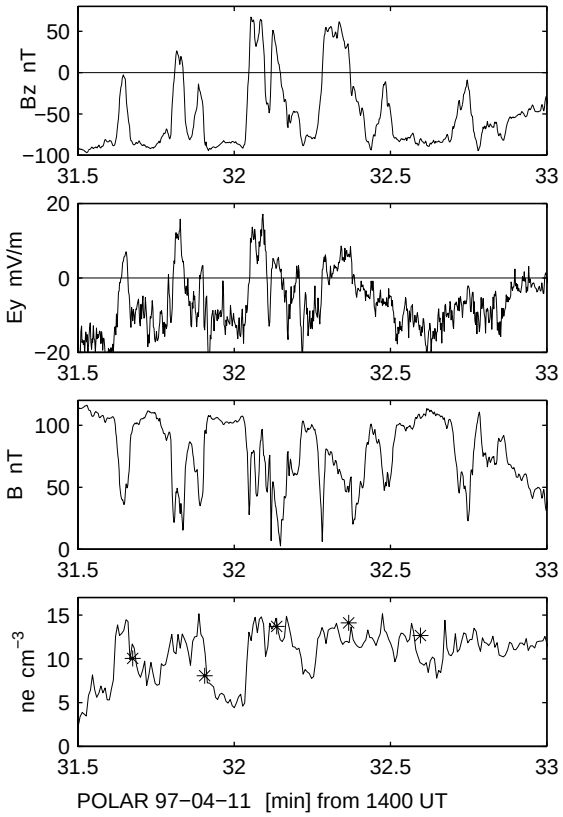

Figure 5. High degree of correlation between perpendicular components of B_z and E_y with $\delta E_y/\delta B_z \approx 200$ km/s $\approx v_A$ indicates Alfvénic structures. The bottom panel shows the electron density derived from the satellite potential (solid line) and from particle measurements (asterisk)

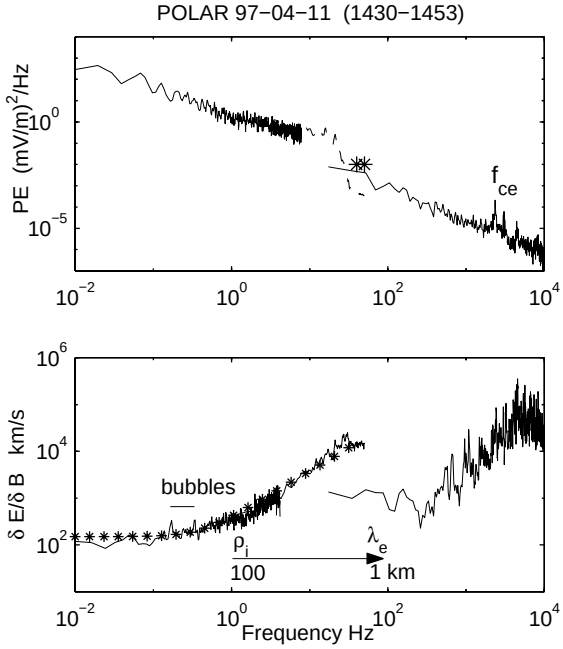

Figure 6. Power spectrum of the electric field fluctuations and the ratio $\delta E/\delta B$ in the magnetic bubble regions. The asterisk plot shows equation (7) computed for $v_A = 150$ km/s and $\rho_i/v = 0.4$ s.

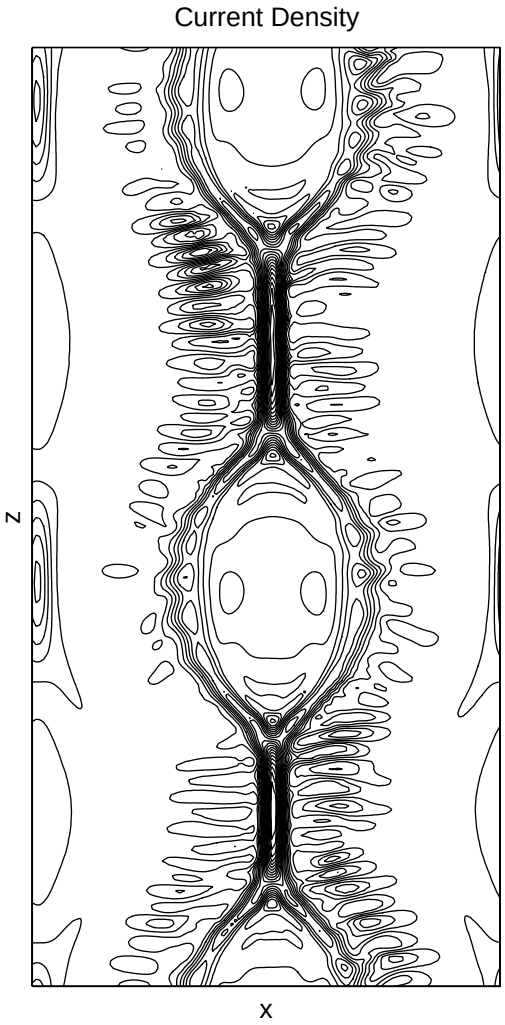

Figure 7. Current density contours taken at time 100 showing the region of most intense current which bounds the magnetic bubble/island region.

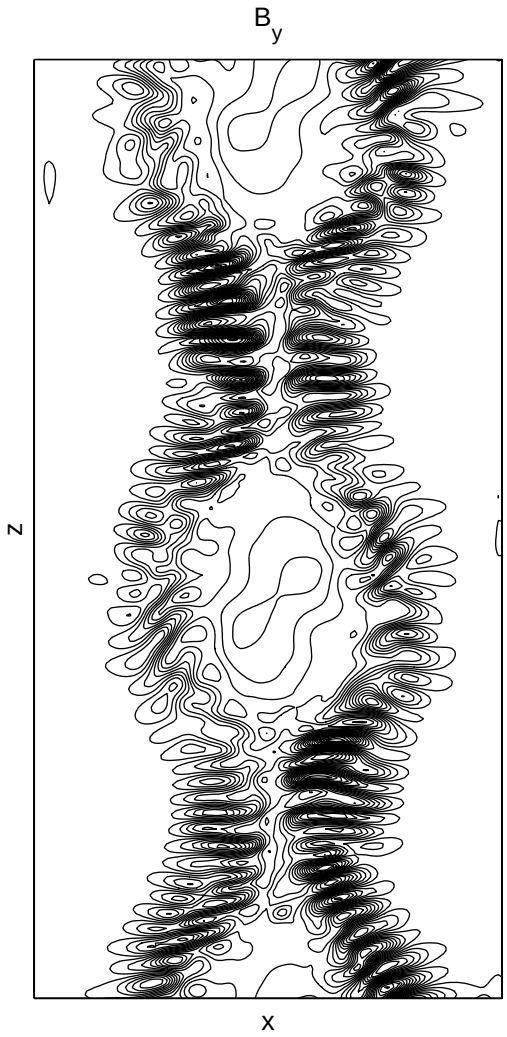

Figure 8. Contour plot of the B_y magnetic field at time 100 showing the fluctuations due to the drift-Alfvén mode which is also an indication of the electron flow.

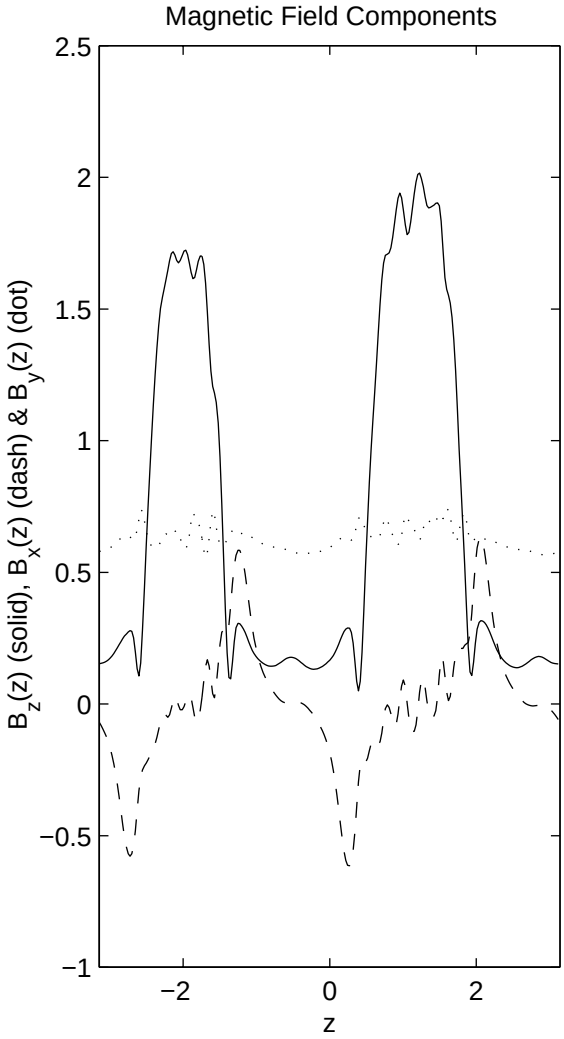

Figure 9. Magnetic field components at time 100 taken along z at a point in x four grid points to the right of the centerline of the simulation. The magnetic bubble region is clearly revealed as the region of minimum B_z. The fluctuations in the field are due to the drift-Alfvén instability.

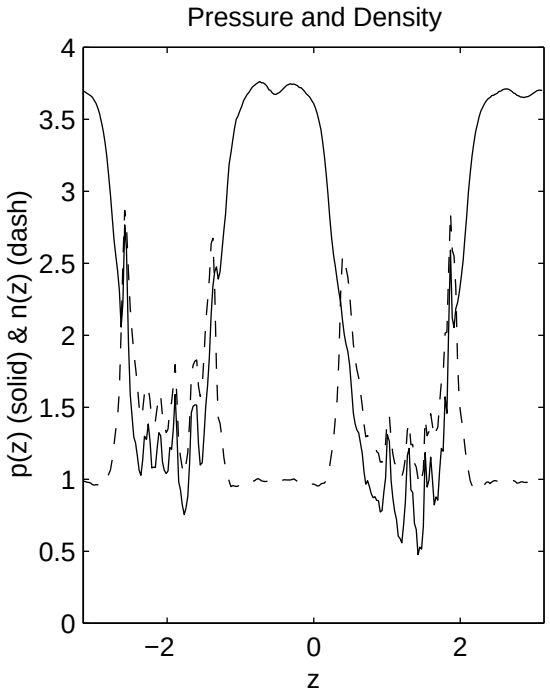

Figure 10. Pressure and density at the same time and location as in figure 9. The region of highest pressure corresponds to the region within the magnetic bubble and is where the temperature is maximum.